Ultramicroscopy 287 (2026) 114444

Contents lists available at ScienceDirect

Ultramicroscopy

journal homepage: www.elsevier.com/locate/ultramic

Noise correlation and phase resolution in off-axis electron holography

Luyang Wang [a,b], Ye Luo [c], Xiaowen Chen [a,b], Xiaoyu Wang [a,b], Wen Shi [a], Jan Caron [d], Thibaud Denneulin [d], Rafal E. Dunin-Borkowski [d], Fengshan Zheng [a,b],*

[a] *Center for Electron Microscopy, South China University of Technology, Guangzhou 511442, China*
[b] *Spin-X Institute, School of Physics and Optoelectronics, Guangdong-Hong Kong-Macao Joint Laboratory of Optoelectronic and Magnetic Functional Materials, State Key Laboratory of Luminescent Materials and Devices, South China University of Technology, Guangzhou 511442, China*
[c] *School of Future Technology, South China University of Technology, Guangzhou 511442, China*
[d] *Ernst Ruska-Centre for Microscopy and Spectroscopy with Electrons, Forschungszentrum Jülich, 52425 Jülich, Germany*

ARTICLE INFO

Keywords:
Transmission electron microscopy
Off-axis electron holography
Noise
Correlation
Phase resolution
Electromagnetic fields and sources

ABSTRACT

Off-axis electron holography is a quantitative phase contrast technique that allows the measurement of electromagnetic fields both within and around the sample. The sensitivity of the electric and magnetic fields (and sources) is thus largely dependent on the quality of the measured phase. Phase retrieval from holograms is usually achieved by a standard Fourier transform method. The aperture used in the reciprocal-space reconstruction process alters the nature of the noise from independence to correlated among pixels. This correlation is further enhanced if additional operator is used, for example, in the calculation of the charge density using the Laplacian operator, and of the magnetic induction and electric field using the gradient operator on the phase. Therefore, it is of importance to trace the noise and correlation of the phase in the processing of experimental holograms, in order to understand the limit of the noise (phase resolution), and further detect infinitesimal tiny electromagnetic signals. In this work, we systematically analyze the noise and correlation of the phase as a function of a variety of parameters, including the detector, electron dose, reconstruction aperture size, Gaussian smoothing and binning. Furthermore, we also assess the effect of the Laplacian and gradient operators on the phase. In particular, we provide detailed analyses on the possibility of detection of a single electric charge and Bohr magnetron. This finding would provide a solid basis for experimental measurements of very weak electromagnetic signals using off-axis electron holography and other phase contrast techniques in transmission electron microscopy.

1. Introduction

Transmission electron microscopy (TEM) imaging techniques typically record only the intensity of the electron wave transmitted through a specimen, resulting in the loss of the phase information during the imaging process. Electron holography overcomes this limitation by interfering an object wave with a reference wave, thereby enabling the retrieval of both the amplitude and phase of the electron wave [1,2]. Among the various forms of electron holography developed for TEM [3], off-axis electron holography using an electron biprism in the image plane remains one of the most widely used approaches because it provides direct and quantitative access to the phase of the electron wave [4]. This capability has made off-axis electron holography a powerful tool for measuring electrostatic and magnetic fields in materials [5–7], including electrostatic charges [8–10], field-emission phenomena [11,12], semiconductor devices [13,14], nanoscale and atomic-scale magnetic fields [15–17], and topological magnetic spin textures [18–20].

In off-axis electron holography, phase retrieval is typically performed by Fourier-transform-based reconstruction of the recorded interference pattern [21]. The noise present in the hologram is therefore transferred through the reconstruction procedure into the recovered phase and amplitude images. The characteristics of noise in electron holography have been discussed for several decades [22–27], and a number of experimental and instrumental factors are known to influence the phase noise, including detector performance, acquisition time, reconstruction parameters, coherence, and instrumental stability [28–34]. Beyond conventional off-axis holography, related approaches such as energy-filtered electron holography attempts to reduce inelastic scattering (phonons or plasma) contributions to the background in holograms, thereby improving fringe contrast and phase sensitivity [35–42]. It is also worth to note that phase-shifting and double-resolution holography could to some extent ease the need for FFT in the reconstruction of the phase information from holograms, maintaining the spatial

* Corresponding author.
E-mail address: zhengfs@scut.edu.cn (F. Zheng).

https://doi.org/10.1016/j.ultramic.2026.114444
Received 11 May 2026; Received in revised form 21 August 2026; Accepted 28 August 2026
Available online 4 September 2026

resolution though reducing the phase resolution, as high frequency bandwidths are not cut off [43–45].

A straightforward way to reduce the stochastic noise is to increase the exposure time or, more generally, the accumulated electron dose. Under shot-noise-limited conditions, the phase detection limit scales inversely with the square root of the total number of detected electrons [23,26]. In practice, this strategy is widely implemented, often together with real-time or offline correction of specimen drift and fringe drift, so that long-exposure or multi-frame acquisition can be performed more effectively [33,46–52]. Additional denoising methods have also been explored, in particular for post-processing of noisy holograms [53–59].

Recent advances in instrumentation and acquisition strategies have pushed off-axis electron holography to phase resolution in the milliradian and even sub-milliradian range under favorable conditions, for example through highly stable microscopes, long-exposure acquisition, frame averaging, and improved correction of drift and vibrations [33,46,49,51,52]. It is worth to note that simply increasing the electron dose does not eliminate the fundamental limit possibly imposed by the imaging system and/or by the statistical nature of the reconstruction process [30,51,52]. This underlines how demanding it remains to approach the ultimate phase resolution or detection limit of off-axis electron holography. In particular, detecting the electrostatic phase shift associated with a single elementary charge, or the extremely weak magnetic signal associated with a single Bohr Magneton, requires phase resolution of as low as $\frac{2\pi}{10^5}$ radian [26,60]. The challenge is even greater in electron-dose-limited situations, such as in the study of biological specimens, beam-sensitive materials and semiconductors, in which the electron radiation may modify the intrinsic properties of samples [61–64].

An important but less systematically addressed issue is that the noise in the reconstructed phase is generally spatially correlated. Correlations may already arise at the detector level, for example through the detector point spread function or other instrumental effects, and could also be introduced or reshaped by the Fourier based reconstruction itself [10,28–30,32,65]. Further mathematical operations on the correlated phase, such as Gaussian smoothing, pixel binning, and spatial differentiation, may enhance correlation between pixels. This is particularly important in the calculations of physical quantities from the phase. For example, the charge density is related to the Laplacian of the phase, and the in-plane magnetic induction and electric field is proportional to the gradient of the phase. The propagation of spatially correlated noise through such differential operators can therefore strongly influence the detection of weak electromagnetic fields.

Despite extensive prior work on phase noise and phase detection limits, most analyses emphasize the magnitude of the noise and often treat it implicitly as white noise. A quantitative understanding of how spatial correlations are generated during hologram reconstruction, how they evolve during post-processing, and how they affect the propagation of noise into derived electromagnetic quantities is still lacking. In particular, it remains unclear to what extent spatially correlated noise changes the effective sensitivity of gradient- and Laplacian-based measurements compared with uncorrelated noise.

In this work, we therefore systematically investigate the noise propagation in off-axis electron holography from holograms to the reconstructed phase and further to derived physical quantities, as a function of the detector, electron dose, reconstruction aperture size, and mathematical operations. Using numerical simulations and experimental verifications, we show that rather than the detection mode, electron dose or number of frames, the FFT-based reconstruction mostly introduces correlation into the phase and that the correlation plays a decisive role in subsequent mathematical operations, for example in the calculation of physical quantities. We demonstrate that the correlated noise is amplified less strongly by gradient and Laplacian operators than uncorrelated noise, which turns out to be favorable for the measurements of weak electromagnetic signals. In particular, we provide guidelines for the measurement of a single elementary charge and Bohr magneton. These results would provide a quantitative framework for the understanding of the noise propagation and offer practical guidance for the detection of weak electromagnetic signals using off-axis electron holography.

2. Fundamental principles

2.1. Electromagnetic fields

Off-axis electron holography is an interferometric technique that enables the measurement of electromagnetic fields through the phase shift of the electron wave arising from electrostatic potentials and magnetic vector potentials within and around the sample, according to the so-called Aharonov–Bohm effect [2,66]. The phase shift of the electron wave modified by electromagnetic fields can be expressed as follows:

$$\varphi = \varphi_e + \varphi_m = C_E \int V(x,y,z)\,dz - \frac{e}{\hbar}\int \mathbf{A}_z(x,y,z)\,dz, \tag{1}$$

where φ_e, φ_m represents the electrostatic and magnetic contributions to the phase, respectively, x, y are coordinates in the sample plane, z is along the electron-beam direction, the interaction constant C_E depends on the accelerating voltage ($C_E = 6.53 \times 10^6$ rad/(V m) for a microscope accelerating voltage of 300 kV), the electrostatic potential V includes contributions from the mean inner potential, fixed charges, mobile charges, and polarization charges, $\mathbf{A}_z$ is the component of the magnetic vector potential along the electron-beam direction, e is the magnitude of the elementary charge, and $\hbar$ is the reduced Planck's constant.

Using Poisson's equation, $\nabla^2 V = -\rho/\epsilon_0$, the charge density can be directly related to the phase [67]:

$$\rho_p(x,y) = -\frac{\epsilon_0}{C_E}\nabla^2\varphi_e(x,y), \tag{2}$$

where ϵ_0 is the vacuum permittivity, $\rho_p(x,y) = \int \rho(x,y,z)\,dz$ denotes the charge density projected along the beam direction.

Using Maxwell's equation, $\mathbf{B} = \nabla \times \mathbf{A}$, and combining Eq. (1), the in-plane magnetic induction can be obtained from the gradient of the phase:

$$\mathbf{B}_p = (B_{p,x}, B_{p,y}) = \frac{\hbar}{e}\mathbf{z} \times \nabla\varphi_m(x,y) = \frac{\hbar}{e}\left(-\frac{\partial\varphi_m}{\partial y}, \frac{\partial\varphi_m}{\partial x}\right), \tag{3}$$

where $\mathbf{B}_p = \int \mathbf{B}(x,y,z)\,dz$ represents the in-plane magnetic induction projected along the beam direction. Note that the gradient of the phase is also able to calculate the electric field ($\mathbf{E}$) projected along the electron beam direction based on the formula: $\mathbf{E} = -\nabla V$.

The magnetization cannot be directly calculated from the phase, as it is usually associated with a convolution integral from the magnetization to the phase [68]. Instead, the magnetization, $\mathbf{m}$, could be quantified from the phase using the method proposed in Ref. [69]. In this approach, the gradient of the phase is first calculated, and the inductive moment components are obtained by integrating the gradient of the phase in a circular region with a radius of r_m,

$$m_B^x = \frac{\hbar}{e\mu_0}\iint \frac{\partial\varphi_m}{\partial x}\,d^2r, \qquad m_B^y = \frac{\hbar}{e\mu_0}\iint \frac{\partial\varphi_m}{\partial y}\,d^2r. \tag{4}$$

The integration was calculated as a function of r_m, and the resulting $m_B(r_m)$ values were fitted as a function of πr_m^2 using a quadratic extrapolation. The extrapolated value at $r_m = 0$ is then used to calculate the magnetization, $\mathbf{m} = (m_x, m_y)$:

$$m_x = 2m_B^x(r_m = 0), \qquad m_y = 2m_B^y(r_m = 0), \qquad |m| = \sqrt{m_x^2 + m_y^2}. \tag{5}$$

This procedure enables direct quantitation of the magnetization from the phase. As this process involves integration over a certain region, the calculated magnetization is assumed to be less sensitive to the noise in the phase, similarly for the calculation of total charges using the line integral method [10].

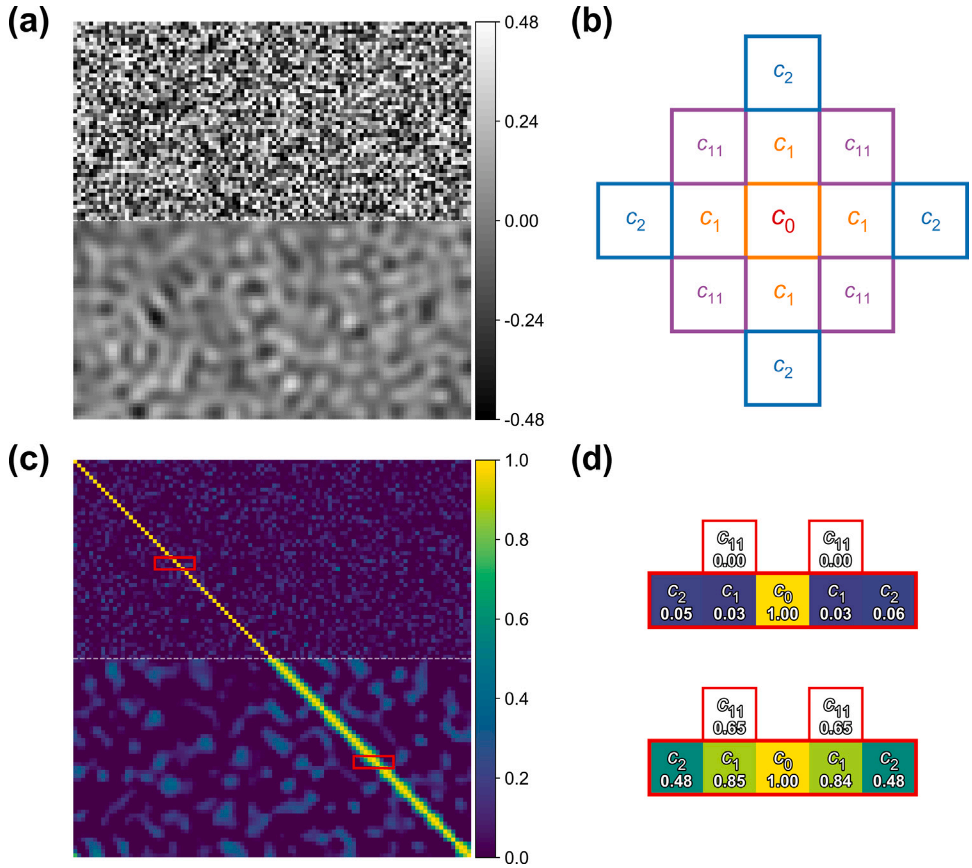

Fig. 1. Representative examples of uncorrelated and correlated noise and their corresponding correlation matrices. (a) White (uncorrelated) noise (top) and synthetic Fourier-filtered correlated noise (bottom). The grayscale bar represents zero-mean noise amplitude in arbitrary units; neither image is a reconstructed phase image. (b) Schematics of correlation coefficients: c_0 (autocorrelation), c_1 (nearest neighbor correlation), c_2 (next nearest neighbor correlation), and c_{11} (diagonal correlation). (c) Corresponding Correlation matrices for the above noise images in (a), and (d) magnified regions around the diagonal (marked by red rectangles) showing the calculated correlation coefficients.

2.2. Noise

The phase resolution, *i.e.*, the noise of the phase, is usually defined as the standard deviation of the phase in a vacuum area, and it could be calculated as formulated below:

$$\delta\varphi = \sqrt{\left\langle (\varphi - \langle\varphi\rangle)^2 \right\rangle}, \tag{6}$$

where $\langle\cdot\rangle$ denotes spatial averaging over a uniform area.

For the shot-noise-limited holograms, the phase resolution both depends on the electron dose and fringe visibility, and can be expressed as follows [23,26,27]:

$$\delta\varphi \propto \frac{\sqrt{2}}{C\sqrt{N}}, \tag{7}$$

where N is the number of detected electrons per pixel, where C is the fringe visibility (see below for definition). It can be seen that the noise decreases with the increase in the electron dose in an inverse-square-root manner, following the stochastic nature of the shot noise.

2.3. Correlation

Spatial correlation may be introduced in hologram acquisition from the detector and in phase reconstruction via the FFT method. Fig. 1a show representative images of uncorrelated and correlated noise. Uncorrelated noise often refers to white noise, where pixels are independent from each other. In a correlated noise image, crosstalk between pixels produces a blurred appearance in neighboring pixels. The two images in Fig. 1a are synthetic noise distributions rather than reconstructed phase images. The uncorrelated image was generated from independent random values, after which the correlated image was obtained by multiplying its Fourier transform by a hard circular low-pass mask with a radius of 0.2 times the image size and applying an inverse Fourier transform. The grayscale bar represents the zero-mean noise amplitude in arbitrary units.

The correlation (covariance) matrix is usually calculated pixel-by-pixel, *i.e.*, every pixel is uncorrelated or correlated with every pixel in the image. To simplify the analysis, we consider only neighboring pixels and use four correlation coefficients: c_0 (autocorrelation), c_1 (nearest neighbor correlation), c_2 (next nearest neighbor correlation), and c_{11} (diagonal correlation), as shown schematically in Fig. 1b. Detailed calculations of these coefficients are provided in Appendix A.

The corresponding correlation matrix is provided in Fig. 1c. Correlated noise broadens the diagonal band of the matrix, demonstrating correlations between neighboring pixels. This is further confirmed by the calculated coefficients shown in Fig. 1d. The correlation coefficients from the nearest, next-to-nearest neighboring pixel increases from almost zero in uncorrelated noise to 0.85 and 0.48 in correlated noise, respectively. The diagonal correlation coefficient then increases from zero to 0.65.

3. Numerical and experimental methods

3.1. Hologram simulation

In simulations, only phase variation was taken into account and amplitude of the electron wave was assumed to be unchanged. The

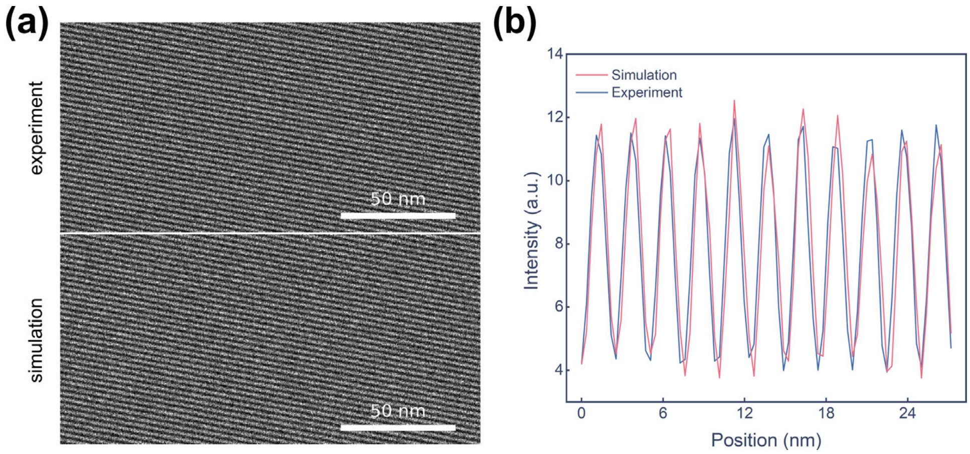

Fig. 2. Quantitative comparison between experimental and simulated results. (a) Experimental (top) and simulated (bottom) holograms with similar acquisition parameters. The experimental hologram was recorded using the K2 counting mode. Electron dose was 10 e⁻/pixel/s, the exposure time was 1 s, the fringe visibility was 50%, the pixel size was 0.36 nm and interference fringe spacing was 2.5 nm. (b) Representative line profiles of the intensity in holograms along the marked lines.

intensity distribution of the hologram could be written below:

$$I(x,y) = N\left[1 + C\cos\left(\frac{2\pi}{s}(x\sin\theta + y\cos\theta) - \varphi_{(x,y)}\right)\right], \quad (8)$$

where N denotes the electron dose (electron counts per pixel), s is the holographic fringe spacing, θ represents the angle between the holographic fringes and the horizontal axis. C is the fringe visibility, and usually accounts for the partial spatial coherence of the electron beam and the detection efficiency of the detector, and could be calculated: $C = \frac{I_{\max}-I_{\min}}{I_{\max}+I_{\min}}$, where $I_{\max}$ and $I_{\min}$ denote the maximum and minimum intensities of the holographic fringes, respectively.

Shot noise was added after calculating the noiseless expected intensity $I(x,y)$ from Eq. (8). For each pixel, $I(x,y)$ was interpreted as the expected number of detected electrons and the recorded integer count was sampled independently as $I_{\text{noisy}}(x,y) \sim \text{Poisson}[I(x,y)]$. The sum of the expected pixel counts therefore defines the expected total number of electrons in the simulated hologram, while the realized total fluctuates according to the independent Poisson samples. Readout noise and dark current noise were not included. This approximation is appropriate for simulations of shot-noise-dominated direct detectors [32,65], *e.g.*, Gatan K2 and Falcon 4i.

3.2. Hologram reconstruction

Hologram reconstruction was performed using the standard Fourier-transform method implemented in the HyperSpy software package [70]. More specifically, the holographic reconstruction was performed using HoloSpy, an extension of the HyperSpy framework. Unless stated otherwise, a circular aperture with a hyperbolic tangent edge profile was used,

$$A(r) = \frac{1}{2}\left[1 - \tanh\left(\frac{r-R}{0.5s}\right)\right], \quad (9)$$

where R is the nominal aperture radius and s is the edge-smoothness parameter. When the parameter `sb_smoothness` is not specified, HoloSpy uses $s = 0.05R$. For all aperture conditions considered below, the inverse Fourier transform was evaluated on an output grid with the same dimensions as the input hologram. Therefore, the observed changes in noise correlation did not result from changes in the number of reconstructed pixels. Unless explicitly stated otherwise, the phase noise standard deviation and the correlation coefficients were calculated from the reconstructed phase images rather than from the holograms. The hologram was first Fourier transformed, and three bands could be identified: a centerband and two conjugate sidebands in the resultant Fourier space. A circular aperture was then used to select one of the sideband. Inverse Fourier-transform was later applied for the selected region, resulting in a real-space complex wave image, where phase and amplitude information were encoded and could be extracted from the modulus and the argument of the complex wave, respectively. It is worth to emphasize that the aperture size not only determines the spatial resolution of the reconstructed images, but also suppresses the noise as high frequency noise in the Fourier space were cut off. Furthermore, correlation between pixels were also introduced by the reconstruction aperture [10,30].

3.3. Experimental setup

Electron holograms were acquired using a Gatan K2 direct electron detector both in linear and counting mode at an FEI Titan HOLO microscope operated at 300 kV [71]. The representative experimental hologram shown in Fig. 2a was recorded using the K2 in counting mode. The electron dose rate was set to 10 e⁻/pix/s with an exposure time of 1 s. The interference fringe spacing was approximately 2.5 nm, the pixel size was 0.36 nm and the fringe visibility was ∼ 50%. The image size was 3710 × 3838 pixels. The central region with a size of 512 × 512 pixels were used to calculate the noise in the phase, in order to exclude the Fresnel fringes from the biprism edges. For better comparison, simulated holograms were also created using similar acquisition parameters, including electron dose, fringe spacing, pixel size, and fringe visibility.

Fig. 2a shows representative experimental and simulated holograms with the same acquisition parameters. The intensity profiles show quantitative agreement, as shown in Fig. 2b. Using the same reconstruction parameters (aperture size was set to half of the carrier frequency), the noises of the phase from experimental and simulated holograms are almost equivalent, 175 mrad and 168 mrad, respectively. The relatively high experimental noise indicates that the holograms contain noise sources in addition to Poisson noise. The correlation coefficients calculated from the reconstructed experimental and simulated phase images are identical, 0.92, 0.73, and 0.85 for c_1, c_2, and c_{11}, respectively. This suggests the reconstruction of the experimental and simulated holograms leads to similar correlations between pixels.

4. From hologram to phase

4.1. Detector

The detector performance, *e.g.*, the modulation transfer, detection quantum efficiency, dark current and readout noise, plays a role in the

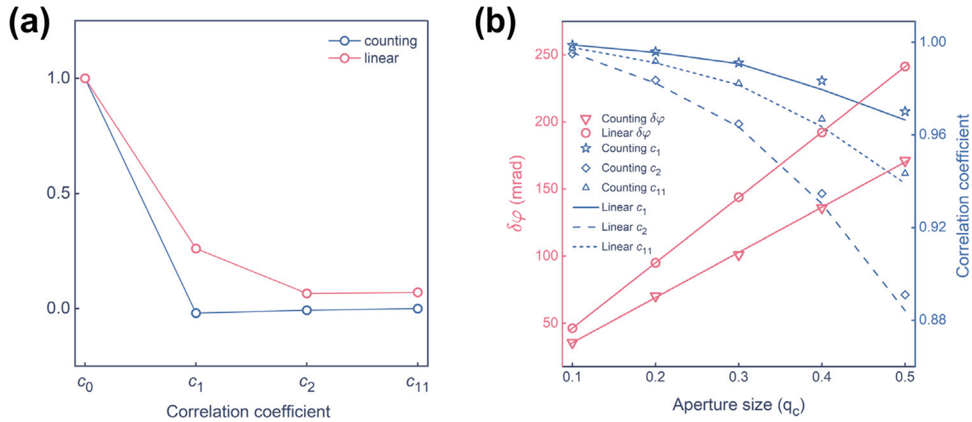

Fig. 3. Noise and correlation coefficients for vacuum data acquired in the counting and linear detector modes. (a) Correlation coefficients calculated directly from the raw white-noise images acquired in vacuum before holographic reconstruction. (b) Phase noise $\delta\varphi$ and spatial correlation coefficients (c_1, c_2, and c_{11}), all calculated from the reconstructed phase images, as a function of the normalized aperture size. The electron dose was 10 e/pixel/s with an exposure time of 1 s. The pixel size was 0.36 nm, the fringe spacing was 2.5 nm, and the fringe visibility was 50% and 45% for the counting and linear modes, respectively.

quality of holograms, in particular in the noise and spatial correlation, as previously discussed in the literature [29,30,32,65].

For indirect detectors, such as scintillator based cameras (*e.g.*, Gatan Ultrascan), signal spreading, optical coupling, and charge sharing introduce interpixel crosstalk [72,73], which can lead to correlated noise already in the recorded holograms. On the other hand, direct electron detectors can suppress these effects more effectively [72]. In the counting mode, individual electron events are detected and spatially localized, so that interpixel crosstalk is reduced and the noise in the raw holograms is expected to be closer to uncorrelated shot noise.

Fig. 3 compares the noise and spatial correlation coefficients for vacuum data acquired in the counting and linear modes. Fig. 3a shows the correlation coefficients of the white noise images in the vacuum. A clear difference is observed: in the counting mode, the correlation coefficients are close to zero, whereas in the linear mode, noticeable correlations remain, reflecting the stronger detector induced crosstalk between pixels, in particular the nearest neighboring pixels (c_1).

Fig. 3b shows the noise and the correlation coefficients in the phase reconstructed from holograms as a function of the aperture size. Although the reconstructed phase noise $\delta\varphi$ is lower in the counting mode than in the linear mode, the three correlation coefficients become very similar in the two modes after reconstruction. This indicates that the spatial correlation in the reconstructed phase is dominated mainly by the reconstruction process itself, rather than by the detector mode. In other words, although the raw holograms acquired in the two modes exhibit different correlation levels, this difference becomes much less pronounced after phase reconstruction.

4.2. Electron dose

We then evaluated the effect of the electron dose on the phase noise and correlation, as it is the most widely used method to suppress the noise in the phase. In practice, the electron dose could be increased either by recording a single hologram at a long exposure time, or by recording multiple holograms [33,46].

Fig. 4a shows the phase noise and correlation coefficients, calculated from the reconstructed phase image, as a function of electron dose for a single simulated hologram. It is seen that the phase noise decreases with the increase of the electron dose, following the inverse-square-root law. Cumulative electron dose by averaging multiple holograms also reports a similar manner, see Fig. 4b. This suggests that the Poisson noise in the hologram alone would not suffice to explain the fundamental limit of the phase resolution reported previously [51,52].

On the other hand, all three correlation coefficients increase $\sim 5\%$ until reach a constant with the increase of the electron dose for a single hologram. This increase suggests that an extremely high intensity would increase the crosstalk between neighboring pixels. The plateau at electron doses greater than 2 e^-/nm^2 indicates that the reconstruction process introduces correlations between pixels, whereas the simulated holograms containing Poisson noise were uncorrelated. In the case of accumulative electron dose, the correlation coefficients stay the same as those in the individual hologram, suggesting multiple hologram averaging does not introduce additional correlation.

4.3. Reconstruction aperture size

As discussed in the above section, the reconstruction process introduces correlation to the phase, it is therefore worth to investigate the effect of reconstruction parameters on the correlation coefficients. We focus primarily on the aperture size (R), as shown schematically in Fig. 5a. q_c denotes the carrier frequency of the interference fringes.

Representative reconstructed phase noise images for two aperture sizes are shown in Fig. 5b. The input phase was spatially uniform and equal to zero; consequently, the phase noise was obtained by subtracting the input phase from the reconstructed phase and removing its spatial mean. The phase noise standard deviation $\delta\varphi$, evaluated over the complete 512 × 512 reconstructed phase image according to Eq. (6), is 0.91 mrad for $R = 0.1q_c$ and 4.35 mrad for $R = 0.5q_c$. For visualization, each phase noise image was divided by its own standard deviation; hence, the grayscale colorbar represents the dimensionless quantity $\varphi/\delta\varphi$ and does not represent the absolute noise amplitude. The corresponding row–row Pearson correlation matrices are displayed on a scale from 0 to 1, where the width of the bright band around the main diagonal indicates the spatial extent of the noise correlation.

Fig. 5 presents the phase noise as a function of the reconstruction aperture size. It is seen that the phase noise increases approximately linearly with the increase of the aperture size. This implies that a smaller aperture would cut off high frequency noise and lead to a suppressed noise in the reconstructed phase, whereas the spatial resolution of the reconstructed images would be compromised, as it equals to the inverse of the aperture size.

Furthermore, the three correlation coefficients (c_1, c_2 and c_{11}) all decrease with the increase of the aperture size in a quadratic-like manner, see Fig. 5. This suggests that a smaller aperture size would enhance the correlation between pixels in the reconstructed images. The phase noise images and correlation matrices in Fig. 5b,c provide a direct visualization of this behavior; the independent normalization of the two phase noise images preserves their spatial texture while their absolute amplitudes are reported separately above. The smaller aperture produces smoother phase noise and a much broader bright

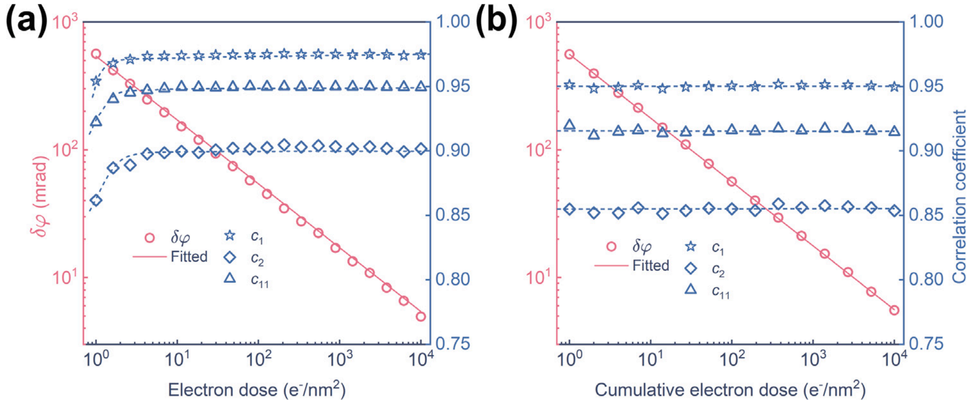

Fig. 4. Phase noise and correlation coefficients calculated from reconstructed phase images as a function of electron dose: (a) A single simulated hologram at each dose; (b) averaging multiple independently simulated holograms, each with an electron dose of 1 e^{-}/nm^2. The simulated hologram each was 512 × 512 pixels, the fringe spacing was 7 nm and the visibility was 50%. Reconstruction aperture size was set to $q_c/2$.

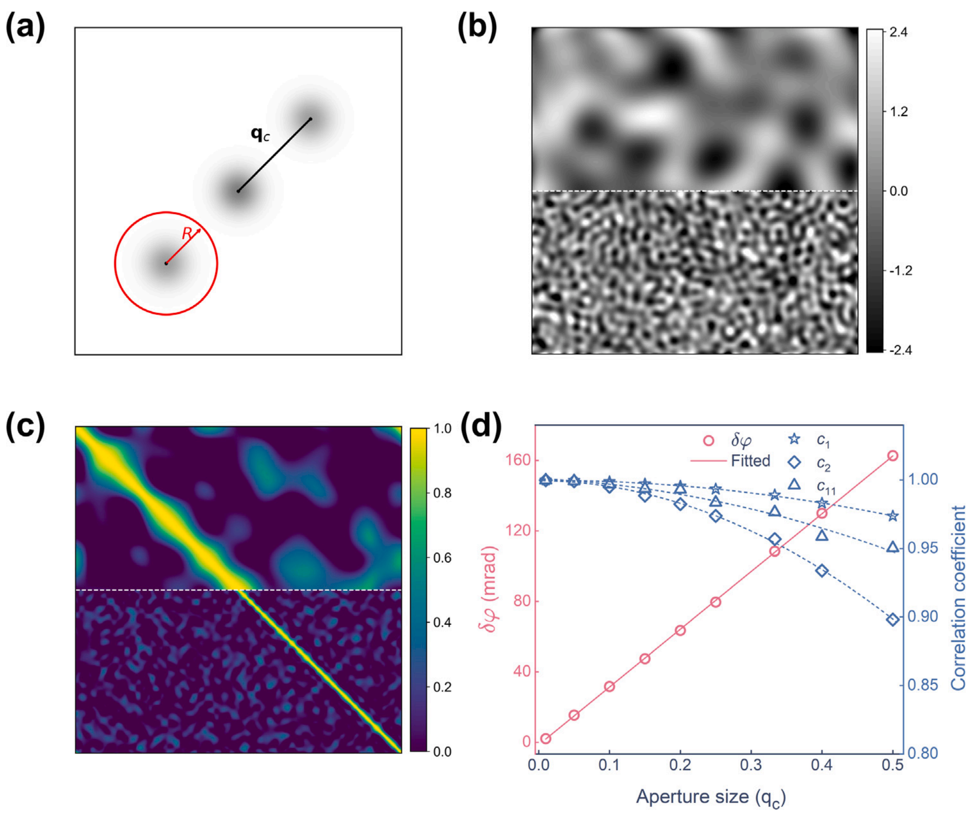

Fig. 5. Effect of reconstruction aperture size on phase noise and spatial correlation. (a) Schematic illustration of the carrier frequency (q_c) and aperture size (R) in the Fourier-transformed hologram. (b) Normalized phase noise images for $R = 0.1q_c$ (top) and $R = 0.5q_c$ (bottom). (c) Corresponding row–row Pearson correlation matrices. (d) Phase noise (left axis) and correlation coefficients (right axis) as a function of the aperture size.

band around the main diagonal of the correlation matrix, whereas the larger aperture produces finer noise and a narrower diagonal band. This reflects the longer-range pixel correlation and reduced effective spatial resolution associated with a small reconstruction aperture. It is also worth to note the correlation coefficients are not smaller than 0.9, even at a aperture size of half of the carrier frequency. The correlation coefficients increase by less than 10% as the aperture size approaches zero.

4.4. Reconstruction-aperture type and edge smoothness

In addition to its radius, both the aperture type and its edge smoothness can affect the phase noise amplitude and spatial correlation. To isolate these effects from the dependence on aperture size discussed above, the nominal aperture radius was fixed at $R = 0.5q_c$, corresponding to $R = 31.82$ pixels under the specified simulation conditions. The same noisy object and reference holograms, simulated at 10 electrons per pixel, were reconstructed for all conditions, and ten independent Poisson-noise realizations were evaluated. We first compared hard circular, hyperbolic tangent, and twelfth order Butterworth apertures. We then used the Butterworth order $n = 4$, 6, 8, 10, and 12 to vary the edge smoothness while keeping the nominal aperture radius fixed. A lower order produces a softer edge with broader transmission tails, whereas a higher order approaches the hard-edge limit.

As shown in Fig. 6a and b, the hard, hyperbolic tangent, and twelfth order Butterworth apertures yielded phase noise standard deviations of

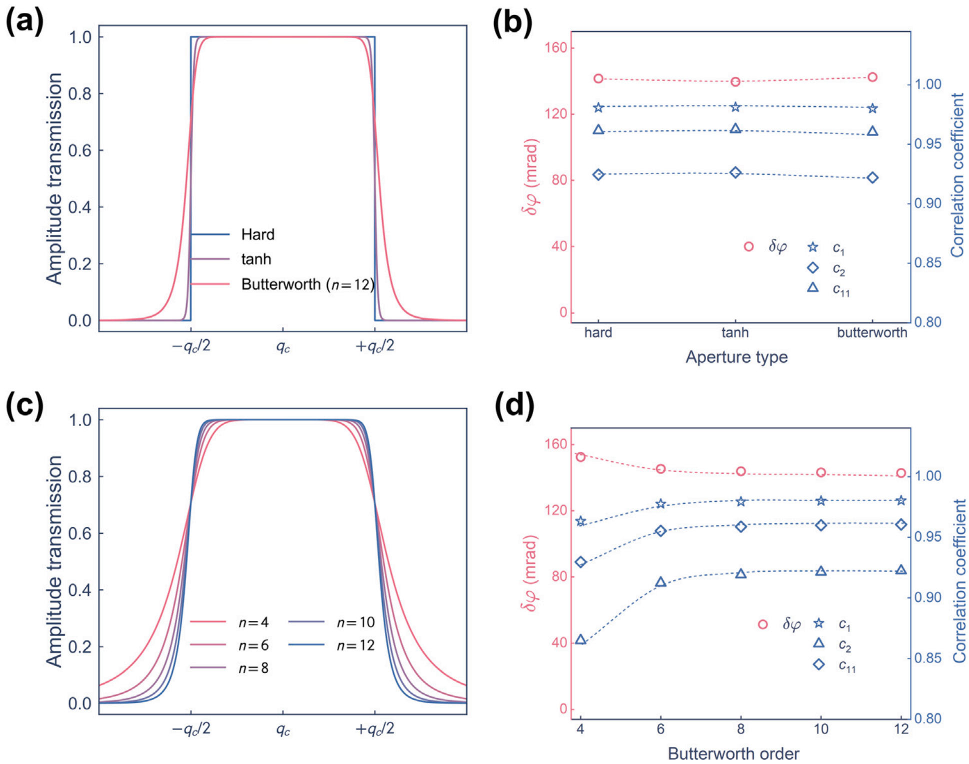

Fig. 6. Influence of reconstruction aperture type and edge smoothness at a fixed reconstruction aperture size ($R = 0.5q_c$). (a) Amplitude transmission for hard, hyperbolic tangent, and Butterworth apertures, and (b) corresponding phase noise and correlation coefficients in the reconstructed phase images. (c) Amplitude transmission for Butterworth apertures with different orders, and (d) corresponding phase noise and correlation coefficients in the reconstructed phase images.

141.6, 139.6, and 142.5 mrad, respectively. Their correlation coefficients were also similar, showing that apertures with comparably sharp edges give nearly the same noise behavior at a fixed nominal radius. The Butterworth-order comparison in Fig. 6c,d shows a stronger effect for a very soft edge: increasing n from 4 to 12 reduced the phase noise from 152.5 to 142.9 mrad, while c_1, c_2, and c_{11} increased from 0.9632, 0.8650, and 0.9296 to 0.9802, 0.9225, and 0.9605, respectively. Most of the change occurred between $n = 4$ and 6, whereas the results for $n =$ 8–12 were close. Thus, broad transmission tails increase the effective passband, transmit more noise, and weaken spatial correlation; once the aperture edge is sufficiently sharp, its precise shape has only a minor influence. Therefore, both the nominal aperture radius and the edge profile should be reported in quantitative phase noise analyses.

4.5. Fringe spacing and Gaussian smoothing

As discussed above, the reconstruction aperture size would introduce correlation into the phase. The carrier frequency corresponds to the fringe spacing of holographic fringes in real space. A small fringe spacing gives rise to a large carrier frequency and *vice versa*. The aperture size is then able to be modified, leading to changes in the correlation coefficients in the phase. Therefore, we then investigated the effect of the fringe spacing on the correlation efficient in the reconstructed phase.

Fig. 7a shows the simulated results as a function of the fringe spacing. The aperture size was set to half of the carrier frequency. It is obvious that the phase noise decreases inversely with the increase of the fringe spacing, indicating a linear increase with the increase of the carrier frequency. This is expected as with a larger fringe spacing, a smaller aperture size is then used for the reconstruction.

This also then explains the increase of correlation coefficients with the increase of the fringe spacing, see blue symbols in Fig. 7a. It also highlights the fact that a large enough fringe spacing (small enough carrier frequency) would lead to fully correlated between adjacent pixels in the phase. This is also consistent with the behavior shown in Fig. 5.

We then tested the effect of Gaussian smoothing on the correlation coefficients of the phase, as it is widely used smoothing technique in noise suppression. The kernel size is fixed to 3 × 3. The smoothing strength is used as the free parameter.

Fig. 7b shows the results as a function of the Gaussian smoothing strength. It is seen that the phase noise is effectively suppressed as the smoothing strength increases, as the updated value of the phase in each pixel was (Gaussian) averaged from the neighboring pixels (the kernel size), and the noise in each pixel would be averaged out to some extent, depending on the smoothing strength. Instead, the correlation coefficients display little dependence on the smoothing strength. This is anticipated that the used kernel size was small and only the nearest, next-to-nearest and diagonal pixels would contribute to the correlation, and these adjacent pixels were already considered in the reconstruction process. It is also worth to note that the use of Gaussian smoothing would sacrifice the spatial resolution of the reconstructed phase.

4.6. Laplacian and gradient

Similarly to Gaussian smoothing, differential operators, including Laplacian and gradient, are also associated with operations between pixels, which inevitably introduce correlation in the resultant images. In addition, as presented above, these differential operators are often used in the calculations of physical quantities. Therefore, in this section, we evaluate the effect of Laplacian and gradient operators on the correlation coefficients and on the noise in the calculated physical quantities.

A discrete Laplacian operator can be expressed in the 3 × 3 matrix form:

$$\nabla^2 \Rightarrow \begin{bmatrix} 0 & 1 & 0 \\ 1 & -4 & 1 \\ 0 & 1 & 0 \end{bmatrix}. \tag{10}$$

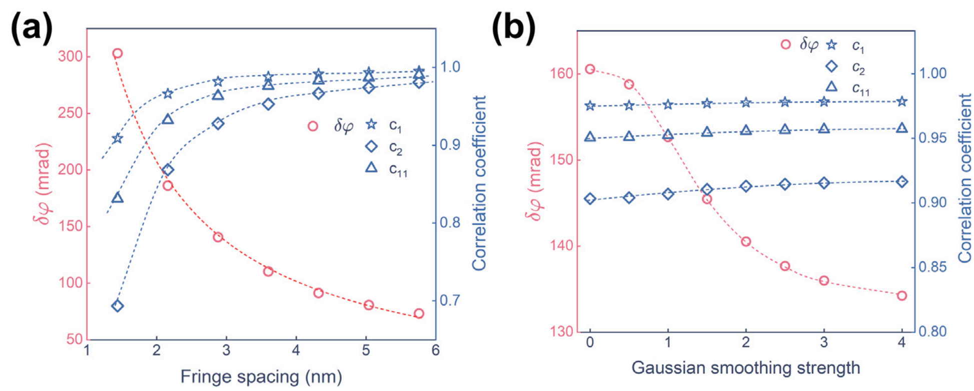

Fig. 7. Phase noise and correlation coefficients as a function of fringe spacing (a) and Gaussian smoothing. Reconstruction aperture size was set to half of the carrier frequency in all cases. The Gaussian kernel size was fixed to 3 × 3.

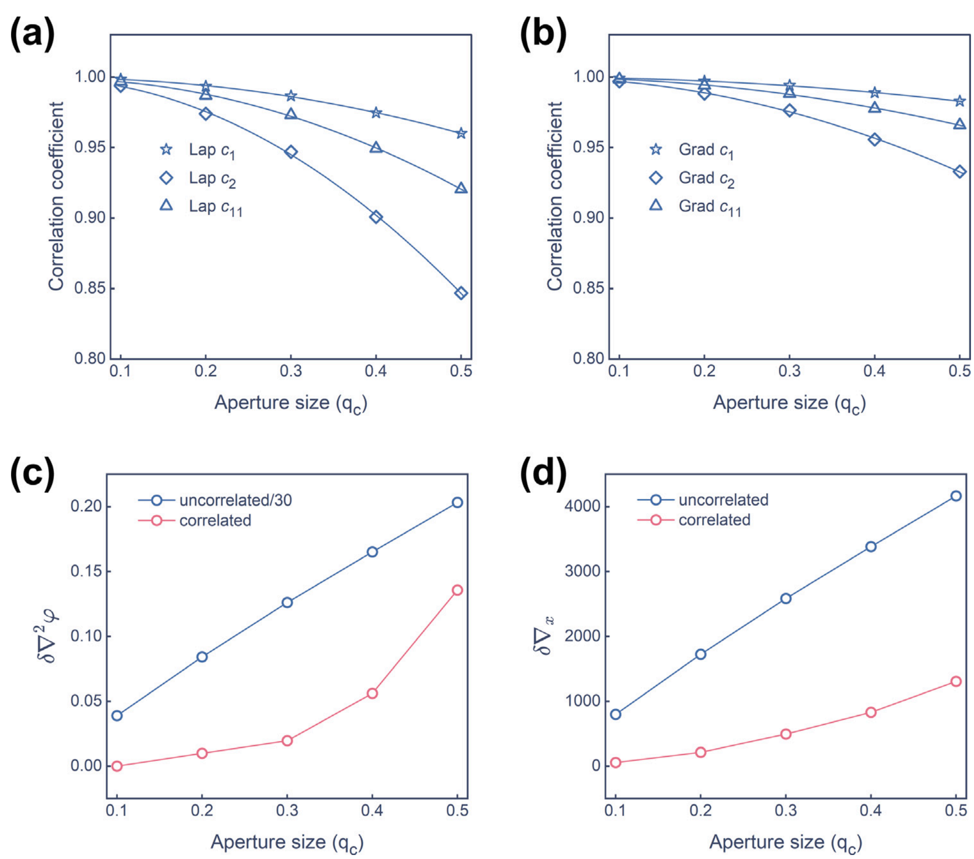

Fig. 8. Laplacian and gradient operations on the correlation and noise as a function of the aperture size. (a) and (b) Correlation coefficients c_1, c_2, and c_{11} after applying the Laplacian and gradient operators to the correlated phase images, respectively. (c) and (d) Noises in the Laplacian- and gradient-operated-phase images, respectively. Noises without taking the correlation into account are also plotted for comparison. For clarity, the uncorrelated noise in c is shown after division by a factor of 30.

The noise in the resultant image after applying the Laplacian operator is $\sqrt{20}$ times that of the original image for uncorrelated noise. When the Laplacian operator is applied to a correlated image, the noise in the resultant image becomes $\sqrt{20-32c_1+8c_{11}+4c_2}$ times that of the original image. According to Eq. (2), the noise in the calculated charge density from the Laplacian of the phase can be written explicitly as follows [10]:

$$\delta\rho = \frac{\varepsilon_0}{C_E}\frac{\sqrt{20-32c_1+8c_{11}+4c_2}}{p^2}\,\delta\varphi, \tag{11}$$

where p is the pixel size.

Similarly, the gradient operator can be represented by the central difference scheme (shown for the x direction only):

$$\nabla_x \Rightarrow \frac{1}{2}\begin{bmatrix}-1 & 0 & 1\end{bmatrix}. \tag{12}$$

For uncorrelated noise, the noise in the resultant image after applying the central-difference operator is $\sqrt{1/2}$ times that of the original image. When the operator is applied to a correlated image, the noise in the resultant image becomes $\sqrt{(1-c_2)/2}$ times as that of the original image. According to Eq. (3), the noise in the calculated magnetic induction field from the gradient of the phase can be written as

$$\delta B_x = \frac{\hbar}{e}\frac{\sqrt{(1-c_2)/2}}{p}\,\delta\varphi. \tag{13}$$

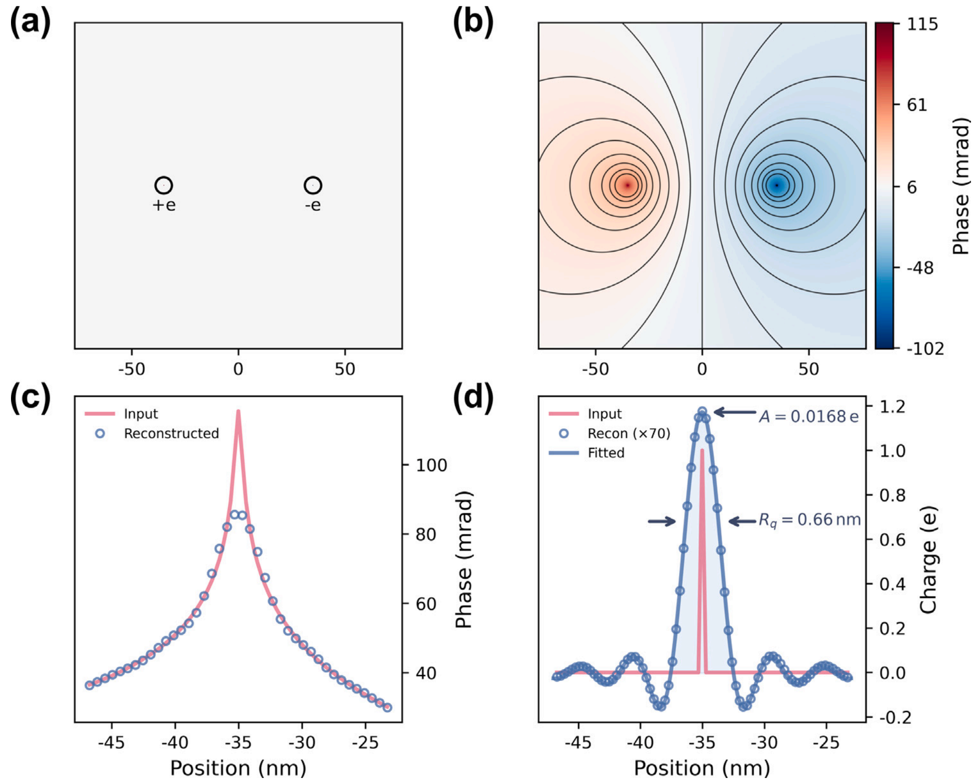

Fig. 9. Detection of an individual elementary charge using off-axis electron holography. (a) Schematic illustration of an electric dipole composed of a single positive and negative elementary charge, with a separation distance of 70 nm. (b) Corresponding theoretical phase shift. The contour spacing is 6 milliradians. (c) Line profiles between the input (theoretical) and reconstructed phase shifts along the horizontal axis across the center of the positive charge. (d) Line profiles between the input and reconstructed (Laplacian) charges along the horizontal axis across the center of the positive charge. For clarity, the reconstructed charge is amplified 70 times.

Fig. 8a and b show the correlation coefficients after applying the Laplacian and gradient operators to the correlated phases as discussed in Section 4.3 and Fig. 5, respectively. For both operators, the correlation coefficients decrease monotonically with the increasing aperture size, indicating that the weaker correlation in the phase images would also be weaker correlations after differential operators. In comparison with the correlation in the phase (see Fig. 5), it can be seen that the Laplacian operators weakens the correlation, whereas the gradient operators strengthens the correlations. This is probably due to the involved neighboring pixels in the operations, as clearly pointed out by the matrix forms.

The noise in the differential-operated images are then calculated from the standard deviation, similarly for the phase image, as shown by red profiles Fig. 8c and d. The noise without correlation is calculated for comparisons (see blue profiles). It is obvious that the correlation lowers the noise both for Laplacian and gradient operators, as also suggested by Eqs. (11) and (13). For the Laplacian operator, the noise is significantly suppressed, probably due to the strong correlation between the nearest-neighbor pixels ($c_1 = 0.96$). This suggests that correlation in the phase would affect strongly the charge calculation from the Laplacian operator (see Eq. (2)). For the gradient operator, as the difference is performed over the next-to-nearest-neighbor pixels, the suppression is only dependent on c_2. A larger c_2 will give rise to a lower noise in the resultant image.

5. From phase to physical quantity

5.1. Elementary charge

We used an electric dipole model to evaluate whether an individual elementary charge could be detected using off-axis electron holography under the specific simulated imaging and reconstruction conditions considered in this study. The electric dipole was composed of one positive and one negative elementary charges with a separation distance of 70 nm, see Fig. 9a. The corresponding phase shift was then calculated, as shown in Fig. 9b. Please see Appendix B for the calculation details. It is seen that the phase shows a typical dipole-like pattern and the maximum phase shift is around 130 mrad.

The calculated phase was then used to simulate holograms. The size of hologram was 512 × 512 pixels with a pixel size of 0.36 nm, indicating the size of the field of view was ~ 184 nm × 184 nm. The fringe spacing was 2.5 nm and the fringe visibility was 50%. The electron dose was 10^5 e^-/pixel. No noise was included such that the results could reflect the intrinsic effect of the reconstruction process. An aperture size of half of the carrier frequency was used for the hologram reconstruction.

Fig. 9c shows quantitative comparison between the input and reconstructed phase line profiles along the horizontal axis across the center of the positive charge. Good agreement is obtained except near the center of the charge. This is mainly due to the limited spatial resolution imposed by the aperture size in the reconstruction. We then used the Laplacian operator to calculate the charge density from the reconstructed phase. Fig. 9d shows direct comparison between the input and reconstructed charge along the horizontal axis across the center of the positive charge. It is seen that the input charge is confined to a single pixel, whereas the reconstructed charge is distributed over a finite area. In addition, in the position where the elementary charge locates, the reconstructed value is around 0.016 e^-, far below the input value.

To quantify this spatial distribution effect, the one-dimensional line profile of the reconstructed charge was then fitted using a modified Airy

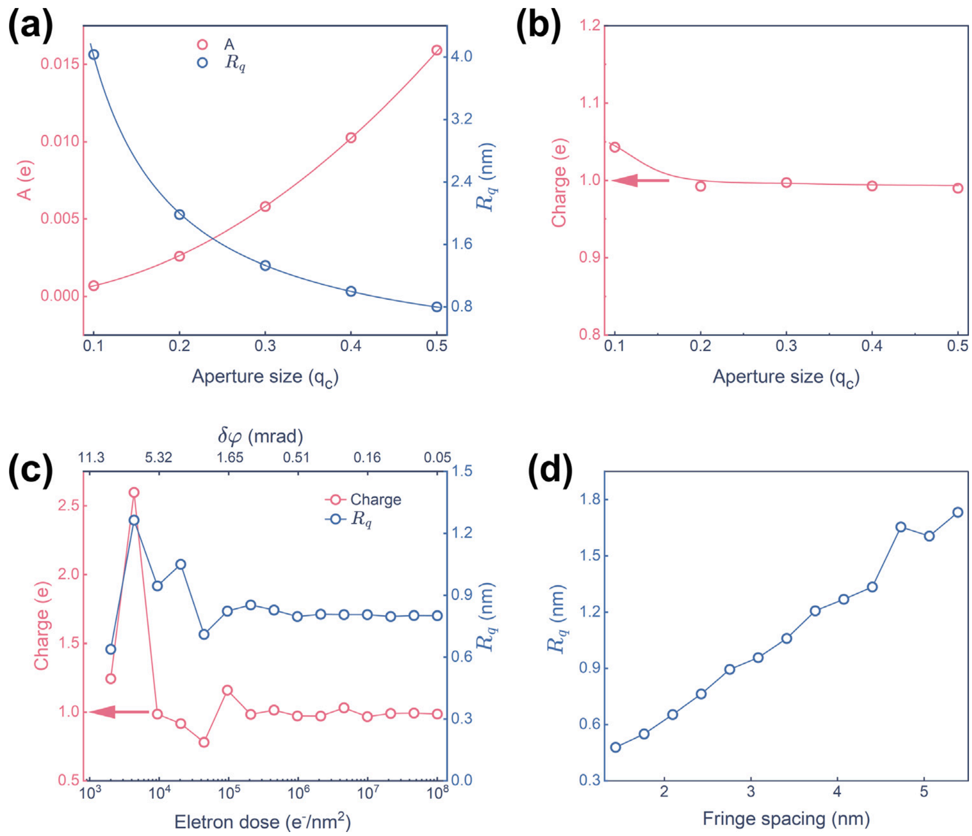

Fig. 10. Quantitative evaluation of the elementary charge measurement using the point spread function. (a) The fitted amplitude (A) and characteristic radius (R_q) as a function of the aperture size. (b) The integrated reconstructed charge as a function of the aperture size. (c) The reconstructed charge and the fitted characteristic radius as a function of the electron dose. Poisson noise was included in the hologram simulations. The upper horizontal axis indicates the corresponding phase noise $\delta\varphi$. (d) The fitted characteristic radius as a function of fringe spacing. Reconstruction aperture size was set to half of the carrier frequency in cases shown in (b) and (c). Reconstruction aperture size was set to half of the carrier frequency in cases shown in (c) and (d). The arrows indicate the expected amount of the charge, 1 e^-.

function,

$$q(x) = A \cdot \frac{2J_1(r/R_q)}{r/R_q} + c, \tag{14}$$

where $q(x)$ is the one-dimensional charge distribution along the horizontal axis, A is the amplitude of the charge, R_q is the characteristic radius, and c is the offset. The fitted profile (blue line in Fig. 9d) well reproduces the broadening and the surrounding oscillatory side lobes, suggesting that the reconstructed charge could be described by the modified Airy function, acting as the so-called point spread function (PSF) of an elementary charge.

We then analyzed the dependence of the aperture size on the elementary charge measurement. It is seen that with the increase of the aperture size, the amplitude (A) increases and the characteristic radius (R_q) decreases, see Fig. 10a. This suggests that with a smaller aperture size (larger correlation between pixels), the elementary charge will diffuse outside, *i.e.*, a smaller amplitude and a large characteristic radius.

The reconstructed charge was then defined to the charges fall within the area between the main lobes (shadowed area in Fig. 9d). A background correction was applied using the fitted offset. Since the reconstructed profile contains negative part, the integration of the reconstructed charge was then normalized. Please see detailed calculation of the reconstructed charge in Appendix C. Fig. 10b shows the reconstructed charge as a function of the aperture size. It is worth to emphasize that the magnitude of the elementary could be reliably reconstructed when the aperture size is not smaller than $0.2q_c$. Under the specified simulation conditions and integration procedure, this result indicates that the aperture primarily broadens the spatial charge distribution rather than preventing recovery of its integrated magnitude.

We then evaluated the accuracy of charge detection as a function of the phase noise by tuning the electron dose, as shown in Fig. 10c. It is seen that the reconstructed charge and characteristic radius of the PSF is not much dependent on the electron dose (phase noise), when the electron dose is greater than 10^5 e⁻nm², or $\delta\varphi$ is lower than 1.65 mrad. This indicates that the phase noise (electron dose) does not change the diffusive behavior of the measurement. The characteristic radius depends strongly on the aperture size, which was fixed to half of the carrier frequency in this analysis.

In order to verify this, we then tested the dependence of the fringe spacing on the charge measurement, see Fig. 10d. Obviously, as the fringe spacing increases, the carrier frequency and the aperture size then decreases, and the characteristic radius increases. This suggests that the characteristic radius is closely related to the spatial resolution, defined by the inverse of the aperture size. When the fringe spacing is sufficient small, the characteristic radius could be as small as one pixel (0.36 nm), *i.e.*, the original size of the input elementary charge.

5.2. Bohr magneton

We examined whether an individual Bohr magneton (μ_B) could be detected using off-axis electron holography under the specific simulated imaging and reconstruction conditions considered in this study. A

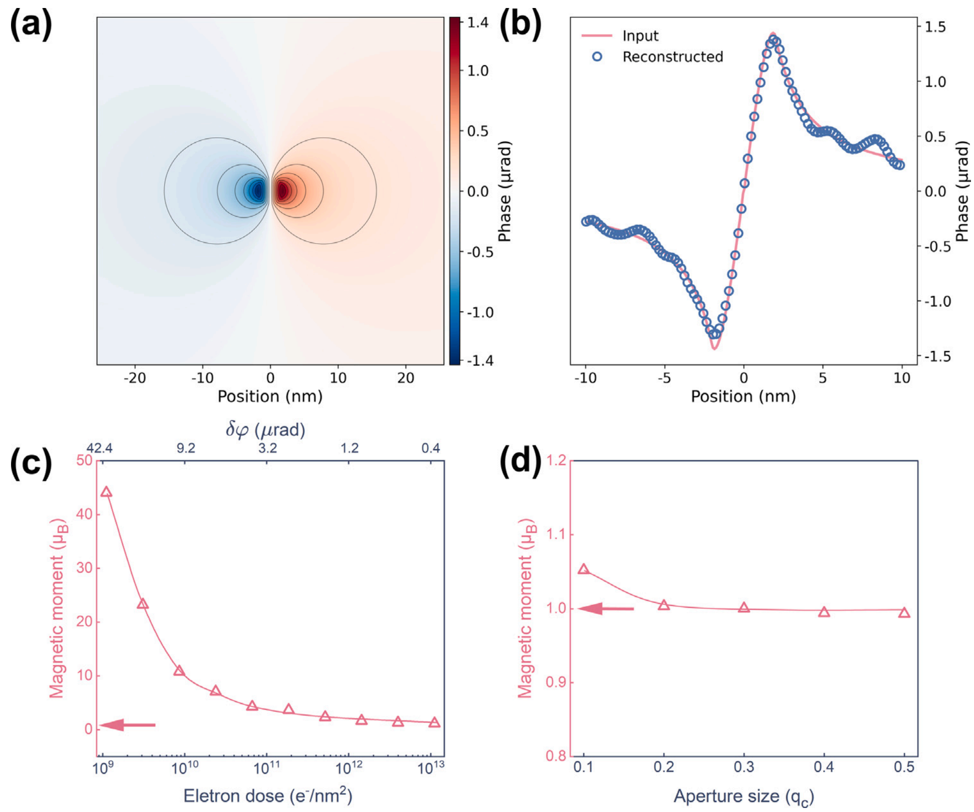

Fig. 11. Detection of an individual Bohr magneton using off-axis electron holography. (a) Theoretical phase shift generated from a magnetic dipole (with 1 μ_B). The contour spacing is 0.18 μradian. (b) Representative line profiles of the theoretical and reconstructed phase shifts. (c) The magnitude of the reconstructed magnetic moment as a function of the electron dose. The upper horizontal axis indicates the corresponding phase noise $\delta\varphi$. (d) The magnitude of the reconstructed magnetic moment as a function of the aperture size. The arrows indicate the expected magnetic moment, 1 μ_B.

magnetic dipole model was used. The phase calculation is described in Appendix B. Fig. 11a shows the phase from the magnetic dipole. The maximum phase shift is observed to be in the order of μrad, more than three orders of magnitude lower than that of the electrostatic charge. Fig. 11b shows representative line profiles of the theoretical and reconstructed phase along the horizontal axis across the center of the dipole. This indicates that the magnetic phase can, in principle, be reconstructed under the idealized and high-dose conditions used in the present simulation.

We then examined the dependence of electron dose (phase noise) on the magnitude of the reconstructed magnetic moment, see Fig. 11c. Because the magnetic dipole induces an extremely small phase shift, an electron dose greater than 10^9 e$^-$/nm^2 is required. It is observed that at a low electron dose, the magnitude of the reconstructed magnetic moment exhibits deviation from the input value, until 10^{13} e$^-$/nm^2, where the phase noise corresponds to 0.4 μrad, sufficient enough to resolve the weak signals from the magnetic dipole (see Fig. 11a). Instead at a low dose, the poor phase resolution is not able to distinguish the dipole from the noise (see the corresponding phase noise for the electron dose at the top horizontal axis in Fig. 11c).

The dependence of the aperture size on the magnitude of the reconstructed magnetic moment is plotted in Fig. 11d. As for the elementary charge, the dependence is weak when the aperture size is greater than $0.2q_c$. As discussed above, the method used for the quantification of the magnetic moment involves the integration over a certain area, and this is also the case in the elementary charge, where the reconstructed charge is integrated over the PSF region.

To isolate the effect of magnetic particle size, the magnetic moment was fixed at 1 μ_B and the particle radius was varied while the field of view, hologram parameters and reconstruction aperture ($R = 0.5q_c$) were kept unchanged. No noise was included in this comparison. Fig. 12b shows that the peak phase decreases rapidly as the same magnetic moment is distributed over a larger particle. Fig. 12a further shows that the reconstructed magnetic moment is also affected by the particle radius: the deviation from the input value increases as the particle becomes larger. Therefore, even for a fixed total magnetic moment and unchanged imaging and reconstruction conditions, the physical size of the measured object is an important parameter that influences both the local phase signal and the accuracy of the reconstructed magnetic moment.

5.3. Electric field and charge density of a p-n junction

We finally considered a one-dimensional symmetric abrupt Si *p-n* junction to examine how phase noise magnitude and spatial correlation affect quantities obtained using the gradient and Laplacian operators. The equilibrium junction had equal donor and acceptor concentrations of 5×10^{17} cm^{-3} and a built-in potential of 1.02 V. The projected phase was calculated for a specimen thickness of 100 nm. Fig. 13 compares the theoretical profiles with reconstructions obtained without shot noise, thereby isolating the finite bandwidth effect of hologram reconstruction. The reconstructed phase and electric field closely follow their theoretical profiles, whereas the sharper charge density variation is more sensitive to the finite aperture because it is obtained from the second derivative of phase.

The effects of electron dose and reconstruction aperture were then separated using two controlled comparisons (Fig. 14). In Fig. 14a, the electron dose was varied while the aperture was fixed at $R = 0.5q_c$. Increasing dose reduces the phase noise, while the recovered peak electric field and charge density approach stable values. In Fig. 14b,

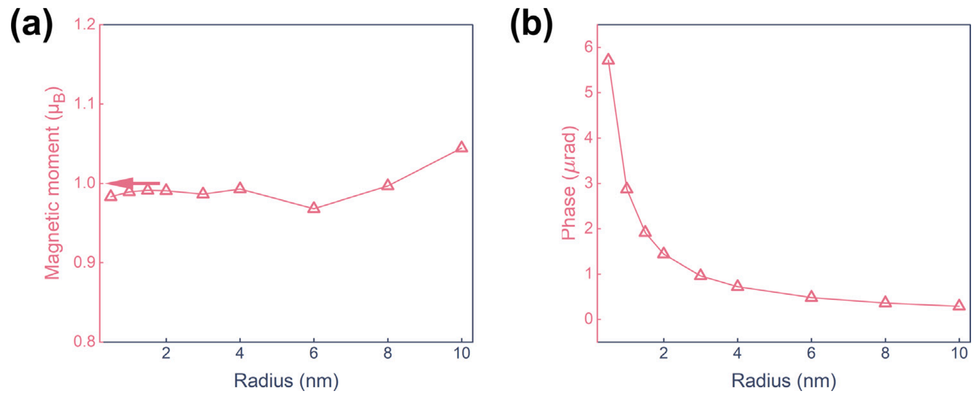

Fig. 12. Effect of magnetic particle radius on the reconstructed magnetic moment. (a) Reconstructed magnetic moment and (b) theoretical peak phase as functions of particle radius.

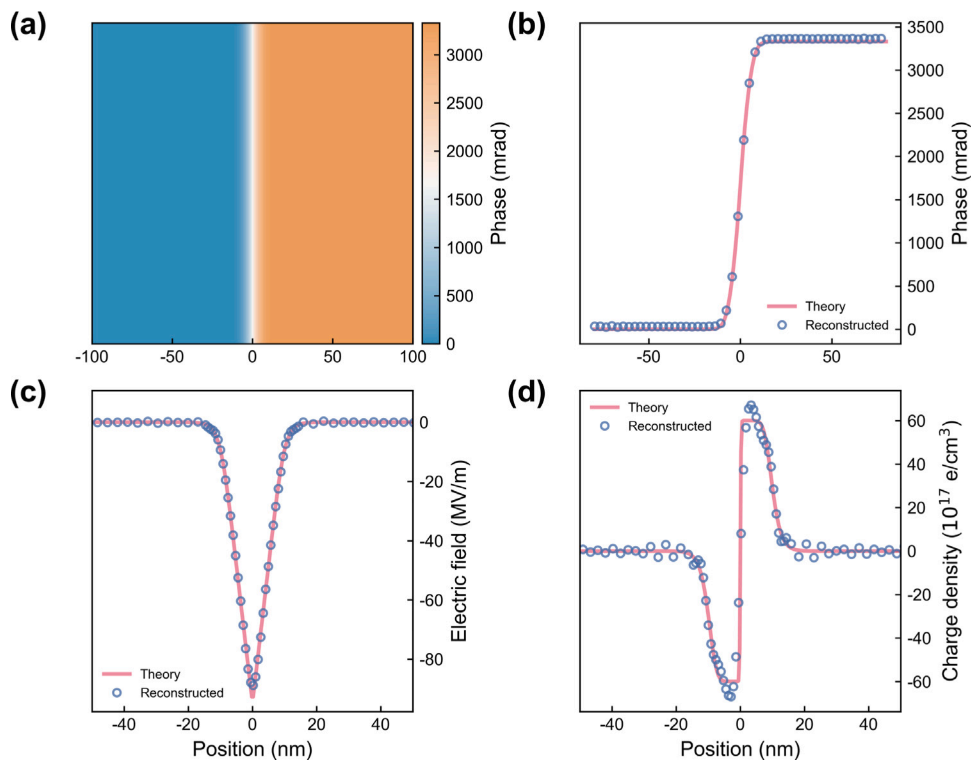

Fig. 13. Model and reconstruction of an unbiased Si *p-n* junction. (a) Theoretical phase image and (b–d) theoretical and reconstructed phase, electric field and charge density profiles.

the aperture was varied from $R = 0.2q_c$ to $R = 0.5q_c$ at a fixed dose of 10^5 e$^-$/nm^2. A smaller aperture increases spatial correlation and suppresses high frequency noise, but also attenuates the sharp charge density response more strongly than the electric field response. Thus, both noise magnitude and spatial correlation must be considered when phase derivatives are used for quantitative *p-n* junction measurements. Only reconstruction-related errors were considered in the present simulations; experimental contributions such as electrostatic fringing fields, surface charges, specimen-preparation damage and irradiation-induced changes were not included. Consequently, the reconstructed profiles remain close to the theoretical results. By contrast, the experimental measurements reported by Yazdi et al. [74] showed much larger discrepancies between theory and experiment as several experimental artefacts and limitations also contributed simultaneously.

6. Conclusions

In summary, we have systematically investigated the noise in off-axis electron holography, with a particular emphasis on correlations introduced by the standard Fourier-based reconstruction method, as a function of the detector, electron dose, reconstruction aperture size, Gaussian smoothing, Laplacian and gradient operators. We show that the aperture size plays a dominant role in the correlation in the phase. Such correlations in the phase will effectively modified the noise in the calculated charge density or electromagnetic field using the differential operators, including Laplacian and gradient operators. We also provide guidelines for the noise and correlation levels required to detect a single elementary charge and a Bohr magneton under the simulated imaging conditions investigated in this study. Overall, this work provides a

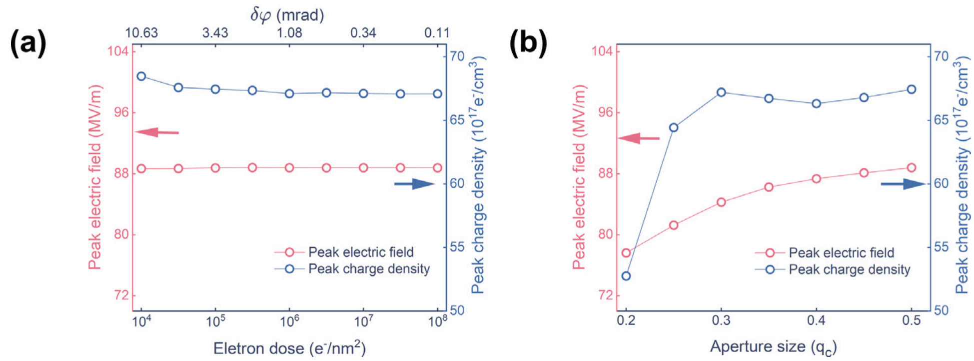

Fig. 14. Effects of (a) electron dose and (b) reconstruction aperture size on the peak electric field and charge density of the *p-n* junction.

quantitative framework and practical guidance for quantitative electron holography of weak electrostatic and magnetic fields.

CRediT authorship contribution statement

Luyang Wang: Writing – review & editing, Writing – original draft, Software, Methodology, Investigation, Formal analysis, Data curation. **Ye Luo:** Validation, Software. **Xiaowen Chen:** Writing – review & editing. **Xiaoyu Wang:** Validation. **Wen Shi:** Writing – review & editing, Validation. **Jan Caron:** Software. **Thibaud Denneulin:** Writing – review & editing, Validation. **Rafal E. Dunin-Borkowski:** Writing – review & editing. **Fengshan Zheng:** Writing – review & editing, Validation, Supervision, Project administration, Funding acquisition, Conceptualization.

Declaration of competing interest

The authors declare that they have no known competing financial interests or personal relationships that could have appeared to influence the work reported in this paper.

Acknowledgments

The authors acknowledge financial support from the National Natural Science Fund (Grant No. 52373226) and for Excellent Young Scientists Fund Program (Overseas), and the National Key R&D Program of China (Grant No. 2024YFA1611100), and the Fundamental Research Funds for the Central Universities. F.Z. is grateful to the GJYC program of Guangzhou (No. 2024D01J0060), the Guangzhou Basic and Applied Basic Research Foundation (No. SL2024A04J00852), the Guangdong Provincial Quantum Science Strategic Initiative (Grant No. GDZX2401002) and the Xiaomi Young Talents Program. R.E.D-B. is grateful for financial support from the European Research Council under the European Union's Horizon 2020 Research and Innovation Programme (Grant No. 856538 - project "3D MAGiC").

Appendix A. Correlation coefficient calculations

Correlation coefficients were evaluated from reconstructed phase images to quantify the spatial correlation of noise. In a standard approach, these coefficients are obtained from a stack of statistically independent images by calculating the Pearson correlation coefficient for each pair of pixels across the stack. However, in the present work only a single phase image is available for each dataset. A modified estimator is therefore adopted.

A.1. Stripe-based correlation estimation

The reconstructed phase image $\phi(x, y)$ is treated as a two-dimensional array of size $N_x \times N_y$. Assuming statistical homogeneity of the noise, each image row is regarded as an independent realization of the same stochastic process. A row–row Pearson correlation matrix is then computed as

$$C(i, j) = \frac{\sum_{k=1}^{N_x} \left[\phi(k, i) - \bar{\phi}_i\right] \left[\phi(k, j) - \bar{\phi}_j\right]}{\sqrt{\sum_{k=1}^{N_x} \left[\phi(k, i) - \bar{\phi}_i\right]^2} \sqrt{\sum_{k=1}^{N_x} \left[\phi(k, j) - \bar{\phi}_j\right]^2}}, \tag{A.1}$$

where i and j denote row indices and $\bar{\phi}_i$ is the mean value of row i.

The correlation coefficients are extracted from the diagonal bands of $C(i, j)$:

- c_0: average of the main diagonal ($i = j$),
- c_1: average of the first off-diagonal bands ($i = j \pm 1$),
- c_2: average of the second off-diagonal bands ($i = j \pm 2$).

To improve statistical robustness, a finite-width diagonal band is used in practice. Specifically, for each valid row index, a five-diagonal window centered on the main diagonal is collected, and the averaged values correspond to $[c_2, c_1, c_0, c_1, c_2]$.

A.2. Estimation of c_{11}

The coefficient c_{11} corresponds to the correlation between diagonal nearest neighbors, i.e. a spatial separation of $\sqrt{2}$ pixels. Since this separation does not correspond to an integer row offset, c_{11} cannot be obtained directly from the row–row correlation matrix.

To estimate c_{11}, the spatial correlation function is assumed to be isotropic and smoothly decaying with distance. It is approximated by a Gaussian form,

$$\rho(r) = A \exp\left(-\frac{r^2}{2\sigma^2}\right), \tag{A.2}$$

where r is the pixel separation. The parameters A and σ are determined by fitting the measured coefficients $\{c_0, c_1, c_2\}$ using nonlinear least squares. The coefficient c_{11} is then obtained by evaluating the fitted function at $r = \sqrt{2}$.

A.3. Rationale for the stripe-based method

The stripe-based estimator replaces ensemble averaging with spatial averaging. Under the assumption that the noise is statistically homogeneous over the selected region, its correlation depends only on the relative pixel separation rather than on absolute position. In this case, different rows provide repeated samples of the same underlying correlation function.

Compared with the conventional stack-based approach, this method enables the estimation of short-range correlation coefficients from a single image while retaining sufficient statistical averaging through the large number of rows. It is therefore suitable for experimental datasets where multiple independent acquisitions are not available.

Appendix B. Phase calculations of dipoles

An ideal electrostatic dipole is constructed from a point charge $q(x_0, y_0, 0)$ and its image charge $q(x_0', y_0', 0)$. The corresponding electrostatic potential is

$$V(x,y,z) = \frac{q}{4\pi\epsilon_0}\left(\frac{1}{\sqrt{(x-x_0)^2+(y-y_0)^2+z^2}} - \frac{1}{\sqrt{(x-x_0')^2+(y-y_0')^2+z^2}}\right). \tag{B.1}$$

The projected phase shift is obtained from the standard phase–potential relation

$$\varphi(x,y) = C_E \int V(x,y,z)\,dz, \tag{B.2}$$

which yields

$$\varphi(x,y) = C_E \frac{q}{4\pi\epsilon_0} \ln \frac{(x-x_0')^2+(y-y_0')^2}{(x-x_0)^2+(y-y_0)^2}. \tag{B.3}$$

The magnetic dipole is modeled as a uniformly magnetized spherical nanoparticle of radius a. The resulting projected phase is expressed as

$$\varphi(x,y) = \frac{e}{\hbar}(k\mu_B)\frac{y}{x^2+y^2}\left[1-\beta(r)\right], \tag{B.4}$$

where the radial coordinate is defined as $r = \sqrt{x^2+y^2}$, and the function $\beta(r)$ describes the finite size of the particle,

$$\beta(r) = \begin{cases} \left(1-\left(\frac{r}{a}\right)^2\right)^{3/2}, & r < a, \\ 0, & r \geq a. \end{cases} \tag{B.5}$$

In this expression, $k\mu_B$ denotes the total magnetic moment, where μ_B is the Bohr magneton and k is the number of magnetic moments (with $k = 1$ corresponding to a single moment).

Appendix C. Charge estimation from the reconstructed charge map

The charge associated with a reconstructed localized peak was estimated by integrating the reconstructed charge map over the main lobe of the peak and applying a correction for the side lobes.

C.1. Method

The reconstructed phase was converted into a reconstructed charge map, whose pixel values are expressed in units of e/pixel. For a localized charge, the reconstructed peak is broadened by the transfer function and is no longer δ-like. A one-dimensional profile through the peak center was fitted using the same functional form as in Eq. (14):

$$q(x) = A \cdot \frac{2J_1(r/R_q)}{r/R_q} + c, \qquad r = |x - x_0|, \tag{C.1}$$

where x_0 the peak position.

The main lobe radius was defined by the first zero of J_1,

$$R_{\mathrm{ml}} = 3.8317\,R_q. \tag{C.2}$$

The charge within the main lobe was then calculated as

$$q_{\mathrm{ml}} = \sum_{(i,j)\in\Omega_{\mathrm{ml}}} q_{ij} - c\,N_{\mathrm{pix}}, \tag{C.3}$$

where Ω_{ml} is the circular region of radius, R_{ml} centered at the peak position, and N_{pix} is the number of pixels inside this region.

Since the assumed response function has negative side lobes, the main lobe integral does not equal the total charge. Within this model,

$$q_{\mathrm{ml}} = \left[1 - J_0(3.8317)\right] q_{\mathrm{true}}, \tag{C.4}$$

with

$$1 - J_0(3.8317) \approx 1.4028. \tag{C.5}$$

The corrected charge estimate is therefore

$$q_{\mathrm{corr}} = \frac{q_{\mathrm{ml}}}{1.4028}. \tag{C.6}$$

C.2. Applicability and limitations

The method is applicable to isolated localized peaks for which the point spread function is approximately isotropic and the peak shape is reasonably described by the function in Eq. (C.1). It further assumes that the local background can be represented by a constant offset.

The limitations are as follows. First, the characteristic radius is obtained from a one-dimensional fit, whereas the charge is determined by two-dimensional integration. Second, the correction factor in Eq. (C.6) is model-dependent and valid only if the reconstructed peak follows the assumed response function. Third, the background subtraction becomes less accurate for non-uniform background or overlapping neighboring peaks. The above procedure should therefore be regarded a model-based estimation of the local charge.

Data availability

Data will be made available on request.

References

[1] D. Gabor, A new microscopic principle, Nature 161 (4098) (1948) 777–778.
[2] H. Lichte, M. Lehmann, Electron holography—Basics and applications, Rep. Progr. Phys. 71 (1) (2008) 016102.
[3] J.M. Cowley, Twenty forms of electron holography, Ultramicroscopy 41 (4) (1992) 335–348.
[4] G. Möllenstedt, H. Düker, Beobachtungen und messungen an biprisma-interferenzen mit elektronenwellen, Z. Phys. 145 (1956) 377–397.
[5] A. Tonomura, Electron holography, in: Springer Series in Optical Sciences, Springer, 1999.
[6] E. Völkl, L.F. Allard, D.C. Joy (Eds.), Introduction to Electron Holography, Springer Science & Business Media, 1999.
[7] R.E. Dunin-Borkowski, A. Kovács, T. Kasama, M.R. McCartney, D.J. Smith, Electron holography, in: Springer Handbook of Microscopy, Springer, 2019, pp. 767–818.
[8] C. Gatel, A. Lubk, G. Pozzi, E. Snoeck, M.J. Hytch, Counting elementary charges on nanoparticles by electron holography, Phys. Rev. Lett. 111 (2) (2013) 025501.
[9] M. Beleggia, L. Gontard, R.E. Dunin-Borkowski, Local charge measurement using off-axis electron holography, J. Phys. D: Appl. Phys. 49 (29) (2016) 294003.
[10] F. Zheng, J. Caron, V. Migunov, M. Beleggia, G. Pozzi, R.E. Dunin-Borkowski, Measurement of charge density in nanoscale materials using off-axis electron holography, J. Electron Spectrosc. Relat. Phenom. 241 (2020) 146881.
[11] J. Cumings, A. Zettl, M. McCartney, J. Spence, Electron holography of field-emitting carbon nanotubes, Phys. Rev. Lett. 88 (5) (2002) 056804.
[12] L. de Knoop, F. Houdellier, C. Gatel, A. Masseboeuf, M. Monthioux, M. Hÿtch, Determining the work function of a carbon-cone cold-field emitter by in situ electron holography, Micron 63 (2014) 2–8.
[13] A. Twitchett, R. Dunin-Borkowski, P. Midgley, Quantitative electron holography of biased semiconductor devices, Phys. Rev. Lett. 88 (23) (2002) 238302.
[14] M.R. McCartney, R.E. Dunin-Borkowski, D.J. Smith, Quantitative measurement of nanoscale electrostatic potentials and charges using off-axis electron holography: Developments and opportunities, Ultramicroscopy 203 (2019) 105–118.
[15] T. Matsuda, S. Hasegawa, M. Igarashi, T. Kobayashi, M. Naito, H. Kajiyama, J. Endo, N. Osakabe, A. Tonomura, R. Aoki, Magnetic field observation of a single flux quantum by electron-holographic interferometry, Phys. Rev. Lett. 62 (21) (1989) 2519.
[16] R.E. Dunin-Borkowski, M.R. McCartney, R.B. Frankel, D.A. Bazylinski, M. Pósfai, P.R. Buseck, Magnetic microstructure of magnetotactic bacteria by electron holography, Science 282 (5395) (1998) 1868–1871.

[17] T. Tanigaki, T. Akashi, T. Yoshida, K. Harada, K. Ishizuka, M. Ichimura, K. Mitsuishi, Y. Tomioka, X. Yu, D. Shindo, et al., Electron holography observation of individual ferrimagnetic lattice planes, Nature 631 (8021) (2024) 521–525.
[18] H.S. Park, X. Yu, S. Aizawa, T. Tanigaki, T. Akashi, Y. Takahashi, T. Matsuda, N. Kanazawa, Y. Onose, D. Shindo, et al., Observation of the magnetic flux and three-dimensional structure of skyrmion lattices by electron holography, Nature Nanotechnology 9 (5) (2014) 337–342.
[19] F. Zheng, F.N. Rybakov, A.B. Borisov, D. Song, S. Wang, Z.-A. Li, H. Du, N.S. Kiselev, J. Caron, A. Kovács, M. Tian, Y. Zhang, S. Blügel, R.E. Dunin-Borkowski, Experimental observation of chiral magnetic bobbers in B20-type FeGe, Nature Nanotechnology 13 (6) (2018) 451–455.
[20] D. Wolf, S. Schneider, U.K. Rößler, A. Kovács, M. Schmidt, R.E. Dunin-Borkowski, B. Büchner, B. Rellinghaus, A. Lubk, Unveiling the three-dimensional magnetic texture of skyrmion tubes, Nature Nanotechnology 17 (3) (2022) 250–255.
[21] E. Völkl, L.F. Allard, B. Frost, A software package for the processing and reconstruction of electron holograms, J. Microsc. 180 (1) (1995) 39–50.
[22] H. Lichte, K.-H. Herrmann, F. Lenz, Electron noise in off-axis image plane holography, Opt. (Stuttgart) 77 (3) (1987) 135–140.
[23] H. Lichte, K.-H. Herrmann, F. Lenz, Statistics of phase and contrast determination in electron holograms, Opt. (Stuttgart) 79 (1) (1988) 13–14.
[24] W.J. de Ruijter, J.K. Weiss, Detection limits in quantitative off-axis electron holography, Rev. Sci. Instrum. 64 (5) (1993) 1325–1332.
[25] A. Harscher, H. Lichte, Experimental study of amplitude and phase detection limits in electron holography, Ultramicroscopy 64 (1–4) (1996) 57–66.
[26] H. Lichte, Performance limits of electron holography, Ultramicroscopy 108 (3) (2008) 256–262.
[27] R. Ishikawa, S. Morishita, T. Tanigaki, N. Shibata, Y. Ikuhara, Spatial and phase resolution in electron microscopy, Microscopy 72 (2) (2023) 78–96.
[28] E. Voelkl, Noise in off-axis type holograms including reconstruction and CCD camera parameters, Ultramicroscopy 110 (3) (2010) 199–210.
[29] R.A. McLeod, M. Malac, Characterization of detector modulation-transfer function with noise, edge, and holographic methods, Ultramicroscopy 129 (2013) 42–52.
[30] F. Röder, A. Lubk, D. Wolf, T. Niermann, Noise estimation for off-axis electron holography, Ultramicroscopy 144 (2014) 32–42.
[31] S.L. Chang, C. Dwyer, C.B. Boothroyd, R.E. Dunin-Borkowski, Optimising electron holography in the presence of partial coherence and instrument instabilities, Ultramicroscopy 151 (2015) 37–45.
[32] S.L. Chang, C. Dwyer, J. Barthel, C.B. Boothroyd, R.E. Dunin-Borkowski, Performance of a direct detection camera for off-axis electron holography, Ultramicroscopy 161 (2016) 90–97.
[33] C. Gatel, J. Dupuy, F. Houdellier, M.J. Hÿtch, Unlimited acquisition time in electron holography by automated feedback control of transmission electron microscope, Appl. Phys. Lett. 113 (13) (2018).
[34] M. Hÿtch, C. Gatel, Phase detection limits in off-axis electron holography from pixelated detectors: Gain variations, geometric distortion and failure of reference-hologram correction, Microscopy 70 (1) (2021) 47–58.
[35] H. Lichte, B. Freitag, Inelastic electron holography, Ultramicroscopy 81 (3–4) (2000) 177–186.
[36] C. Boothroyd, R. Dunin-Borkowski, The contribution of phonon scattering to high-resolution images measured by off-axis electron holography, Ultramicroscopy 98 (2–4) (2004) 115–133.
[37] P. Potapov, H. Lichte, J. Verbeeck, D. Van Dyck, Experiments on inelastic electron holography, Ultramicroscopy 106 (11–12) (2006) 1012–1018.
[38] J. Verbeeck, D. Van Dyck, H. Lichte, P. Potapov, P. Schattschneider, Plasmon holographic experiments: Theoretical framework, Ultramicroscopy 102 (3) (2005) 239–255.
[39] P. Potapov, J. Verbeeck, P. Schattschneider, H. Lichte, D. Van Dyck, Inelastic electron holography as a variant of the feynman thought experiment, Ultramicroscopy 107 (8) (2007) 559–567.
[40] F. Röder, H. Lichte, Inelastic electron holography–first results with surface plasmons, Eur. Phys. J.-Appl. Phys. 54 (3) (2011) 33504.
[41] J. Verbeeck, G. Bertoni, H. Lichte, A holographic biprism as a perfect energy filter? Ultramicroscopy 111 (7) (2011) 887–893.
[42] F. Kern, D. Wolf, P. Pschera, A. Lubk, Quantitative determination of elastic and inelastic attenuation coefficients by off-axis electron holography, Ultramicroscopy 171 (2016) 26–33.
[43] Q. Ru, J. Endo, T. Tanji, A. Tonomura, Phase-shifting electron holography by beam tilting, Appl. Phys. Lett. 59 (19) (1991) 2372–2374.
[44] Q. Ru, G. Lai, K. Aoyama, J. Endo, A. Tonomura, Principle and application of phase-shifting electron holography, Ultramicroscopy 55 (2) (1994) 209–220.
[45] V. Volkov, M. Han, Y. Zhu, Double-resolution electron holography with simple Fourier transform of fringe-shifted holograms, Ultramicroscopy 134 (2013) 175–184.
[46] E. Voelkl, D. Tang, Approaching routine $2\pi/1000$ phase resolution for off-axis type holography, Ultramicroscopy 110 (5) (2010) 447–459.
[47] R.A. McLeod, M. Bergen, M. Malac, Phase measurement error in summation of electron holography series, Ultramicroscopy 141 (2014) 38–50.
[48] T. Niermann, M. Lehmann, Averaging scheme for atomic resolution off-axis electron holograms, Micron 63 (2014) 28–34.
[49] V. Boureau, R. McLeod, B. Mayall, D. Cooper, Off-axis electron holography combining summation of hologram series with double-exposure phase-shifting: Theory and application, Ultramicroscopy 193 (2018) 52–63.
[50] Y. Takahashi, T. Akashi, A. Sato, T. Tanigaki, H. Shinada, Y. Murakami, Automated acquisition of vast numbers of electron holograms with atomic-scale phase information, Microscopy 69 (2) (2020) 132–139.
[51] M. Hytch, C. Marcelot, C. Gatel, Phase detection limits in electron holography with automatic stabilisation and direct electron detection, in: BIO Web of Conferences, vol. 129, EDP Sciences, 2024, p. 04004.
[52] T. Denneulin, B. Zingsem, J. Vas, W. Shi, L. Yang, M. Feuerbacher, R.E. Dunin-Borkowski, Acquisition of object and temperature series in medium resolution off-axis electron holography with live drift correction, Ultramicroscopy 271 (2025) 114119.
[53] S. Anada, Y. Nomura, T. Hirayama, K. Yamamoto, Simulation-trained sparse coding for high-precision phase imaging in low-dose electron holography, Microsc. Microanal. 26 (3) (2020) 429–438.
[54] Y. Midoh, K. Nakamae, Accuracy improvement of phase estimation in electron holography using noise reduction methods, Microscopy 69 (2) (2020) 123–131.
[55] Y. Nomura, K. Yamamoto, S. Anada, T. Hirayama, E. Igaki, K. Saitoh, Denoising of series electron holograms using tensor decomposition, Microscopy 70 (3) (2021) 255–264.
[56] T. Tamaoka, Y. Midoh, K. Yamamoto, S. Aritomi, T. Tanigaki, M. Nakamura, K. Nakamae, M. Kawasaki, Y. Murakami, Denoising electron holograms using the wavelet hidden Markov model for phase retrieval—Applications to the phase-shifting method, AIP Adv. 11 (2) (2021).
[57] S. Anada, Y. Nomura, T. Hirayama, K. Yamamoto, Computational evaluation of sparse coding on off-axis electron holograms: Comparison between charge-coupled device and direct-detection device cameras, Microscopy 71 (1) (2022) 41–49.
[58] S. Anada, Y. Nomura, K. Yamamoto, Enhancing performance of electron holography with mathematical and machine learning–based denoising techniques, Microscopy 72 (6) (2023) 461–484.
[59] S. Lee, Y. Midoh, Y. Tomita, T. Tamaoka, M. Auchi, T. Sasaki, Y. Murakami, Noise reduction of electron holography observations for a thin-foiled Nd-Fe-B specimen using the wavelet hidden Markov model, Appl. Microsc. 54 (1) (2024) 4.
[60] H. Lichte, F. Börrnert, A. Lenk, A. Lubk, F. Röder, J. Sickmann, S. Sturm, K. Vogel, D. Wolf, Electron holography for fields in solids: Problems and progress, Ultramicroscopy 134 (2013) 126–134.
[61] P. Simon, H. Lichte, P. Formanek, M. Lehmann, R. Huhle, W. Carrillo-Cabrera, A. Harscher, H. Ehrlich, Electron holography of biological samples, Micron 39 (3) (2008) 229–256.
[62] E. Karim, C. Gatel, A. Leforestier, S. Balor, V. Soldan, C. Plisson-Chastang, P.-E. Gleizes, E. Snoeck, Off-axis electron holography of unstained bacteriophages: Towards electrostatic potential measurement of biological samples, J. Struct. Biol. 217 (1) (2025) 108169.
[63] L. Houben, M. Luysberg, T. Brammer, Illumination effects in holographic imaging of the electrostatic potential of defects and $p-n$ junctions in transmission electron microscopy, Phys. Rev. B 70 (16) (2004) 165313.
[64] J.B. Park, T. Niermann, D. Berger, A. Knauer, I. Koslow, M. Weyers, M. Kneissl, M. Lehmann, Impact of electron irradiation on electron holographic potentiometry, Appl. Phys. Lett. 105 (9) (2014).
[65] P. Grob, D. Bean, D. Typke, X. Li, E. Nogales, R.M. Glaeser, Ranking TEM cameras by their response to electron shot noise, Ultramicroscopy 133 (2013) 1–7.
[66] Y. Aharonov, D. Bohm, Significance of electromagnetic potentials in the quantum theory, Phys. Rev. 115 (3) (1959) 485–491.
[67] M. Beleggia, T. Kasama, R.E. Dunin-Borkowski, S. Hofmann, G. Pozzi, Direct measurement of the charge distribution along a biased carbon nanotube bundle using electron holography, Appl. Phys. Lett. 98 (24) (2011) 243101.
[68] M. Beleggia, Y. Zhu, Electron-optical phase shift of magnetic nanoparticles I. Basic concepts, Phil. Mag. 83 (8) (2003) 1045–1057.
[69] M. Beleggia, T. Kasama, R.E. Dunin-Borkowski, The quantitative measurement of magnetic moments from phase images of nanoparticles and nanostructures—I. fundamentals, Ultramicroscopy 110 (5) (2010) 425–432.
[70] F. de la Peña, E. Prestat, V.T. Fauske, P. Burdet, J. Lähnemann, P. Jokubauskas, M. Nord, T. Ostasevicius, K.E. MacArthur, D.N. Johnstone, M. Sarahan, V. Migunov, A. Eljarrat, J. Caron, T. Furnival, J. Barthel, M. Séverin, M. Walls, N. Cautaerts, HyperSpy: A multi-dimensional data analysis toolbox, 2022.
[71] C. Boothroyd, A. Kovács, K. Tillmann, FEI titan G2 60-300 HOLO, J. Large-Scale Res. Facil. 2 (2016) A44.
[72] G. McMullan, A.R. Faruqi, D. Clare, R. Henderson, Comparison of optimal performance at 300 keV of three direct electron detectors for use in low dose electron microscopy, Ultramicroscopy 147 (2014) 156–163.
[73] A.R. Faruqi, G. McMullan, Direct imagers for electron microscopy, Nucl. Instrum. Methods Phys. Res. Sect. A 645 (1) (2011) 29–34.
[74] S. Yazdi, T. Kasama, M. Beleggia, M. Samaie Yekta, D.W. McComb, A.C. Twitchett-Harrison, R.E. Dunin-Borkowski, Towards quantitative electrostatic potential mapping of working semiconductor devices using off-axis electron holography, Ultramicroscopy 152 (2015) 10–20.